

Topological electronic states in holey graphyne

Yong-Cheng Jiang,^{†,‡} Toshikaze Kariyado,[†] and Xiao Hu^{*,†,‡}

[†]*Research Center for Materials Nanoarchitectonics (MANA), National Institute for
Materials Science (NIMS), Tsukuba 305-0044, Japan*

[‡]*Graduate School of Science and Technology, University of Tsukuba, Tsukuba 305-8571,
Japan*

E-mail: HU.Xiao@nims.go.jp

Abstract

We unveil that the holey graphyne (HGY), a two-dimensional carbon allotrope where benzene rings are connected by two $-\text{C}\equiv\text{C}-$ bonds fabricated recently in a bottom-up way, exhibits topological electronic states. Using first-principles calculations and Wannier tight-binding modeling, we discover a higher-order topological invariant associated with C_2 symmetry of the material, and show that the resultant corner modes appear in nanoflakes matching to the structure of precursor reported previously, which are ready for direct experimental observations. In addition, we find that a band inversion between emergent g -like and h -like orbitals gives rise to a nontrivial topology characterized by \mathbb{Z}_2 invariant protected by an energy gap as large as 0.52 eV, manifesting helical edge states mimicking those in the prominent quantum spin Hall effect, which can be accessed experimentally after hydrogenation in HGY. We hope these findings trigger interests towards exploring the topological electronic states in HGY and related future electronics applications.

Haldane was the first to notice that a typical topological state, i.e., quantum Hall effect, can be realized without Landau levels induced by an external magnetic field. He developed a tight-binding (TB) model on honeycomb lattice with complex next-nearest-neighbor hoppings which break time-reversal symmetry (TRS) but introduce no net external magnetic field, generating quantum *anomalous* Hall effect characterized by a Chern number.¹ Although this toy model was thought to be unrealistic at the time of the original proposal, soon after the discovery of graphene² it was pointed out by Kane and Mele that if spin-orbit coupling (SOC) is taken into account, graphene can be regarded as two copies of Haldane model, one for up spin and the other for down spin, manifesting the TRS-preserved quantum *spin* Hall effect (QSHE) characterized by a \mathbb{Z}_2 invariant^{3,4} (see also Ref. 14). However, the predicted QSHE is extremely hard to observe experimentally in graphene because of its very weak SOC. In order to resolve this issue, honeycomb systems with heavy elements have been investigated, aiming at having stronger SOC. Recently large-gap QSH insulators have been realized, in Bismuthene,⁶ monolayer 1T'-WTe₂,⁷ stanene⁸ and ultrathin Na₃Bi⁹ for instance. For monolayer 1T'-WTe₂ with an energy gap ~ 55 meV,¹⁰ the quantized edge conductance was observed in a transport channel of 100 nm up to 100 K;⁷ while for the other materials, although energy gaps range from 0.3 eV to 0.8 eV, evidence for nontrivial topology is still limited in showing the local density of states (LDOS) for edge states, partially due to their small sample sizes below 40 nm. Despite all the noticeable progresses, further investigations are needed on materials possessing sizable energy gaps and amenable to fabrication into structures for device applications.

Besides utilizing strong SOC, deforming honeycomb lattice while preserving C_{6v} crystalline symmetry is also able to open a sizable gap in the Dirac dispersion associated with graphene structure, where the band inversion between bands with *p*- and *d*-like characters generates nontrivial topology.¹¹⁻¹³ This idea has been experimentally verified first in photonic crystals¹⁴⁻¹⁸ due to their comparably easy fabrication, and later in electronic systems using *molecular graphene*,¹⁹ which is constructed by aligning carbon-monoxide molecules regularly

on the Cu(111) surface in terms of the scanning tunneling microscopy (STM) technique.^{20,21} Such a superstructuring with C_{6v} symmetry can also generate corner modes originating from higher-order topology (HOT),²² which has been observed in photonic crystals,²³ various metamaterials²³⁻²⁸ and electronic artificial lattices.²⁹ However, delicate deformations at the angstrom scale in real electronic materials are extremely difficult. While it was proposed that graphene with nanohole arrays¹² might reduce the difficulty, so far the top-down approach has not succeeded in fabricating nanohole arrays with desired patterns and scales. As the alternative approach, bottom-up synthesis methods have been tried, such as graphene nanoribbon,³¹ nanoporous graphene³² and graphyne^{33,34} with atomic precision, which yield interesting electronic³⁵⁻³⁸ and mechanical properties.³⁹

Here, we unveil topological electronic states in the holey graphyne (HGY) fabricated recently in a bottom-up way⁵ using first-principles calculations and Wannier TB modeling.⁴¹ HGY is a two-dimensional (2D) carbon allotrope where benzene rings are connected by two $-C\equiv C-$ bonds (Figure 1A). A nontrivial higher-order topological invariant is obtained from the C_2 symmetry of the material, and the resultant corner modes appear in nanoflakes with the edge morphology matching to the structure of precursor,⁵ which are ready for direct experimental observations. In addition, we find that intriguing molecular orbitals emerge in the hexagonal unit cell, and specially a band inversion between g -like and h -like modes gives rise to a nontrivial topology characterized by the \mathbb{Z}_2 topological invariant. In order to observe the helical edge states similar to those in QSHE, we propose in-plane hydrogenation in HGY to absorb the $p_{x,y}$ orbitals of carbon atoms in the pristine material, which opens a global topological energy gap at the appropriate energy and makes the helical edge states with opposite orbital angular momenta (OAM) observable in experiments.

By employing density-functional-theory (DFT) calculations (see Supporting Note S1), we obtain the stable real-space structure of HGY with a lattice constant of $a_0 = 10.85 \text{ \AA}$ (see Supporting Note S1) and the band structure as depicted in Figures 1A and 1B, respectively, in good agreement with the results in the previous work.⁵ The structure in Figure 1A can

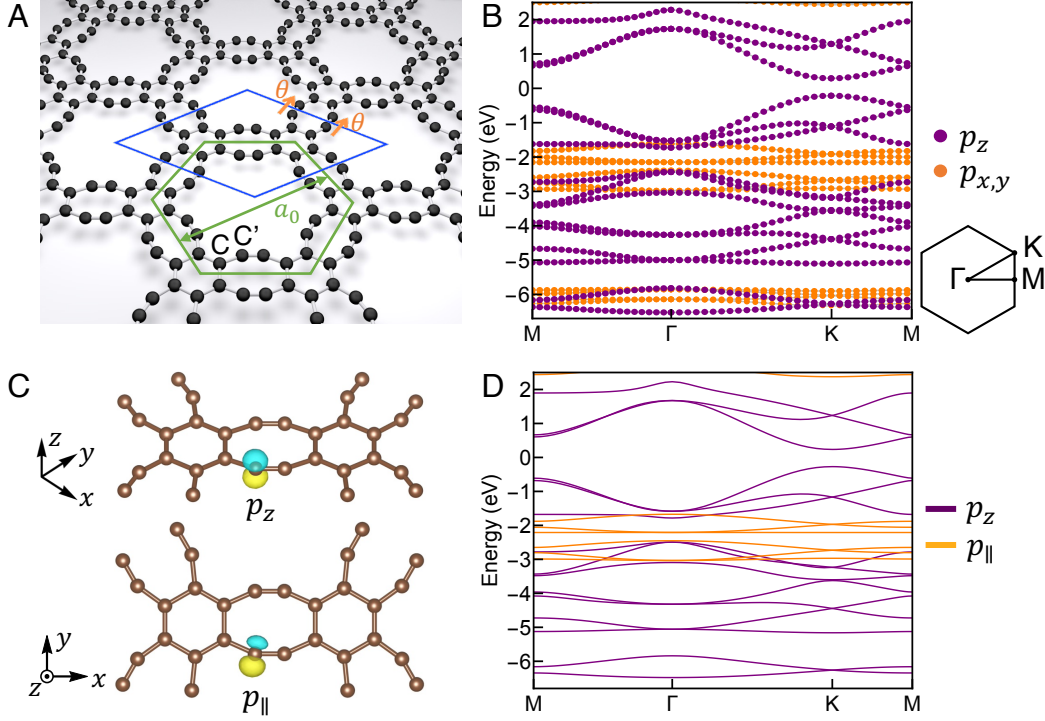


Figure 1. Holey graphyne (HGY) and its band structures. (A) Stable structure of HGY with lattice constant a_0 obtained by DFT calculations. Carbon atoms are divided into two types, C and C', where the former belongs to the benzene rings and the latter only belongs to the octagon. The rhombic unit cell corresponds to the precursor in the bottom-up synthesis as discovered in Ref. 5, whereas the hexagon denotes the highest symmetric unit cell. A pair of twist phases θ are introduced in two sp -hybridized bonds for the calculation on the Berry phase γ for HOTI. (B) DFT band structure and the Brillouin zone. The Fermi energy is set to zero, and the eigenstates are projected to p_z and $p_{x,y}$ orbitals. (C) p_z -like and p_{\parallel} -like maximally localized Wannier functions obtained from the localization procedure, where the p_{\parallel} orbital is the superposition of p_x and p_y orbitals. (D) Wannier-interpolated band structure obtained from the subspace selected by projecting onto p_z orbitals on each atom and p_{\parallel} orbitals on atoms C'.

be regarded as a network of hexagons (benzene rings) and octagons, and there are two types of carbon sites, one belongs to the hexagon (shared with the octagon) and the other only belongs to the octagon. We name the former and the latter C and C', respectively. For the band structure in Figure 1B, we project the eigenstates onto the p_z and $p_{x,y}$ orbitals of carbon atoms, and find that occupations are either zero or unity, indicating no hybridization between them due to the mirror symmetry of the 2D material. The p_z orbital is also found orthogonal to the s orbital, and thus no hybridization occurs between these two orbitals. Therefore, the p_z bands can be treated independently of other bands.

From the C_2 symmetry of the precursor octagon (see Figure 1A), we surmise a HOT in the HGY. In order to explore the possibility, we first employ Wannier localization procedure to obtain the Wannier TB Hamiltonian. According to the orbital occupations shown in Figure 1B, in the Wannierization the eigenstates are projected onto p_z orbitals on each atom, and the resulted maximally localized Wannier function (MLWF) is illustrated in the upper panel of Figure 1C (see Supporting Note S1). The Wannier-interpolated band structure for this p_z -like MLWF is displayed in Figure 1D, which reproduces the p_z bands obtained by DFT calculations shown in Figure 1B.

With the obtained Wannier TB Hamiltonian, we calculate the Berry phase γ for HOT insulator (HOTI)⁴²⁻⁴⁴ associated with a pair of twist phases θ introduced on the double bonds of HGY as depicted in Figure 1A (see Supporting Note S1). The Hamiltonian $H(\theta)$ can be separated into two parts as

$$H(\theta) = h_0(\theta) + h_1, \quad h_0(\theta) = -t \sum_{\langle mn \rangle} (e^{i\theta} c_m^\dagger c_n + e^{-i\theta} c_n^\dagger c_m), \quad (1)$$

where $h_0(\theta)$ with nearest-neighbor hopping energy $t = 3.0$ eV obtained by MLWF is for the part with twist phases and h_1 is for the rest of the system. Note that since the phase twist is applied only on the selected bonds, this phase twist cannot be gauged out. The Berry phase

for HOTI is defined as

$$\gamma = -i \int_0^{2\pi} d\theta \langle \Psi(\theta) | \partial_\theta | \Psi(\theta) \rangle \pmod{2\pi} \quad (2)$$

with $|\Psi(\theta)\rangle$ being the ground state of $H(\theta)$. Since the system has the C_2 symmetry at the center of octagon, γ remains the same when $\theta \rightarrow -\theta$, i.e. $\gamma = -i \int_0^{-2\pi} d\theta \langle \Psi(\theta) | \partial_\theta | \Psi(\theta) \rangle = -i \int_{2\pi}^0 d\theta \langle \Psi(\theta) | \partial_\theta | \Psi(\theta) \rangle \pmod{2\pi}$, where we shift the integration by 2π since $H(\theta) = H(\theta + 2\pi)$. Knowing that the integration over a close loop $\theta = 0 \rightarrow 2\pi \rightarrow 0$ is 0 modulo 2π , γ is a \mathbb{Z}_2 index being either 0 or π . We find out

$$\gamma = \pi \quad \text{at the } \frac{9}{24} \text{ filling of } p_z \text{ bands,} \quad (3)$$

which corresponds to the filling upto the gap at -2.5 eV. Our calculation indicates clearly a nontrivial HOT in the HGY.

The nontrivial HOT will manifest corner modes in flake structures within the topological energy gap of p_z bands, which ranges from -2.5 eV to -1.8 eV. However, as can be seen in Figure 1B, this energy gap is covered by the $p_{x,y}$ bands, which hampers the observation of corner modes if the corner modes and the bulk states of $p_{x,y}$ orbitals are energetically close. Therefore, it is necessary to consider a Hamiltonian which includes those $p_{x,y}$ bands around the energy gap. Again we employ Wannier localization procedure, while this time the eigenstates are projected onto a superposition of p_x and p_y orbitals on atoms C'. The resulted MLWF is illustrated in the lower panel of Figure 1C, which is parallel to the plane of the material and thus named p_{\parallel} . The Wannier-interpolated band structure for this p_{\parallel} -like MLWF, combined with that for the p_z -like MLWF, is displayed in Figure 1D, which matches perfectly with the DFT band structure shown in Figure 1B in the energy range of interest.

Apparently, in the target bandgap of p_z orbital there are finite DOS of p_{\parallel} . In order to observe topological corner states arising from p_z orbital experimentally, the nanoflake should be small enough to have the bulk spectrum discretized, which makes it possible to distinguish

the corner states from bulk states energetically. Here we construct several minimal nanoflakes consisting of three rhombic unit cells with different symmetries which host topological corner states (see other flake structures in Supporting Note S2). The LDOS $|\psi_i|^2$ for the corner states are visualized in Figure 2, with intensity proportional to size of dots. For the straight type in Figure 2A, the corner state is located at the energy of -1.85 eV, with the energy difference of 0.08 eV to bulk states owing to the finite-size effect (see the energy spectrum in Supporting Note S2). This energy difference is large enough for the STM technique to detect the corner states by measuring differential conductance (dI/dV) maps. We anticipate that the differential conductance map will show a similar pattern as illustrated in Figure 2A where electrons mainly locate in the two outmost unit cells. From the inversion symmetry of this nanoflake (i.e. C_2 symmetry), it is expected that two corner states exist: a bonding state and an antibonding state. Here we only show the antibonding state, since in the bonding state the wave functions at two different corners have a strong overlap with each other, making the bonding state difficult to distinguish from bulk states by only seeing LDOS. For the boomerang type-I in Figure 2B, the corner state is at the energy of -1.85 eV, with the energy difference of 0.08 eV to bulk states. For the boomerang type-II in Figure 2C, the corner states are situated at energies of -1.92 eV, -1.84 eV and -1.80 eV, respectively, and the smallest energy gap between the corner states and bulk states is 0.03 eV, which can also be observed experimentally. The two corner states with the lower energies possess opposite mirror eigenvalues (see the wave functions in Supporting Note S2), and their degeneracy is lifted because of the hybridization; while the corner state with the higher energy is a singlet with the wave function localized at the central corner.

We also investigate first-order topology which can be characterized by parity index (C_2 eigenvalue with respect to the center of hexagonal unit cell shown in Figure 1A).⁴⁵ For this purpose, we evaluate the parity index by counting the numbers of parity-even states at both Γ and M points ($N_{\Gamma/M}^+$) for all the valence bands below the global bandgap at -2.4 eV and find $(N_{\Gamma}^+, N_{\text{M}}^+) = (21, 21)$, which apparently suggests that the material is topologically

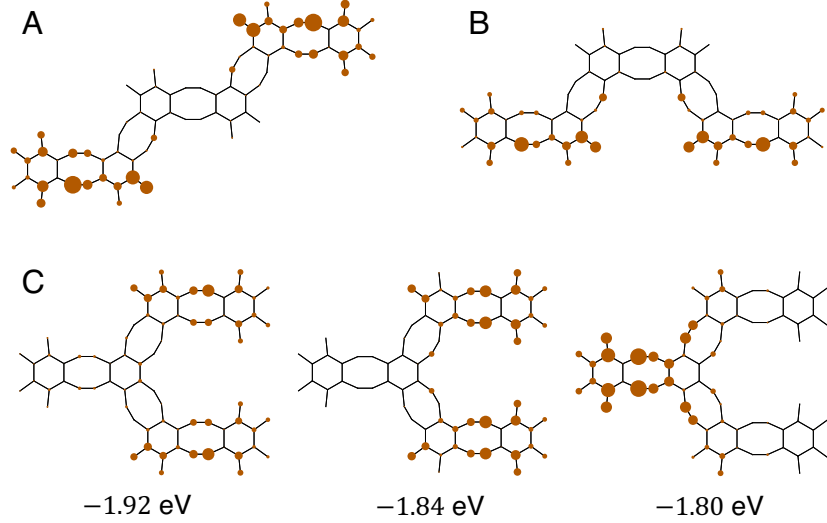


Figure 2. Topological corner modes in nanoflakes of HGY. (A–C) Local density of states (LDOS) $|\psi_i|^2$ for the corner states in all three types of nanoflakes with three rhombic unit cells: (A) straight type, (B) boomerang type-I, and (C) boomerang type-II, with energy -1.94 eV, -1.84 eV and -1.80 eV, respectively.

trivial. However, it turns out that the topology of HGY is much richer than it looks at the first glance.

Since the p_z bands are independent of other bands as discussed in the previous section, we can extract the parity index for the p_z bands which gives $(N_{\Gamma}^+, N_M^+) = (3, 5)$. This imbalance of parity index indicates the presence of nontrivial topology. Meanwhile, the parity index for the other bands, namely s and $p_{x,y}$ bands, is $(N_{\Gamma}^+, N_M^+) = (18, 16)$. By checking the parity index in details, we find out the imbalance originated from the three bands of $p_{x,y}$ orbitals around $E = -3$ eV, which give $(N_{\Gamma}^+, N_M^+) = (3, 1)$. Therefore, HGY hosts two sets of topological bands, one from the p_z orbital and the other from the $p_{x,y}$ orbitals. Namely, these two orthogonal sets of bands exhibit nontrivial topology, showcasing rich topological characteristics in HGY. The Wannier TB model reproduces the parity indices for p_z and $p_{x,y}$ bands obtained by DFT calculations, meaning that it successfully captures the nontrivial topology of the material.

Associated with the imbalance of parity index, we expect that the material manifests topological edge states within the energy gap of p_z bands around -2 eV (see Figure 1B).

Unfortunately, as can be seen in Figure 1D, these edge states are covered in energy by the bulk bands of p_{\parallel} orbital although orthogonal to each other. In order to solve this issue, we consider in-plane hydrogenation on HGY, where hydrogen atoms are attached to carbon atoms C'. The stable structure of hydrogenated HGY (HHGY) with a lattice constant $a'_0 = 11.02 \text{ \AA}$ obtained by DFT calculations is illustrated in Figure 3A (see bond lengths and angles in Supporting Note S1). The DFT band structure is shown in Figure 3B, where a global energy gap of 0.52 eV is opened at the energy of -2 eV compared to the band structure of pristine HGY shown Figure 1B. Similar to the situation in HGY, the p_z bands in HHGY are orthogonal to other bands because of the mirror symmetry with respect to the horizontal plane. Therefore, we perform the Wannierization procedure by projecting the eigenstates onto p_z orbitals on each carbon atom, and the interpolated band structure is shown in Figure 3C, reproducing the p_z bands obtained by DFT calculations shown in Figure 3B.

We display the projected density of states (PDOS) for HHGY in Figure 3D, where the $p_{x,y}$ orbitals of carbon atoms and the s orbital of hydrogen atoms exist below the bandgap at -2 eV . This is in sharp contrast to the situation in HGY where the $p_{x,y}$ orbitals fill up almost all the bandgap of p_z orbital as displayed in Figure 1B. The in-plane hydrogenation leads to the sp -hybridization between the $p_{x,y}$ orbitals of carbon atoms and the s orbital of hydrogen atoms, lowering the energy of the original p_{\parallel} orbital. Therefore, the hydrogenation effectively kills the original p_{\parallel} orbital and results in an energy gap as large as 0.52 eV.

In order to double check our strategy, we re-examine the topology for the p_z bands using parity index, and find imbalance by $(N_{\Gamma}^+, N_{\text{M}}^+) = (3, 5)$ for the states below the energy gap, indicating the presence of nontrivial topology as expected (see Supporting Note S3). We can also check the parity index for all states including other orbitals, which gives $(N_{\Gamma}^+, N_{\text{M}}^+) = (24, 26)$, meaning that the nontrivial topology originates purely from the p_z bands as discussed above.

Moreover, in Figures 3B and 3C we notice that the unbalanced parity index is induced

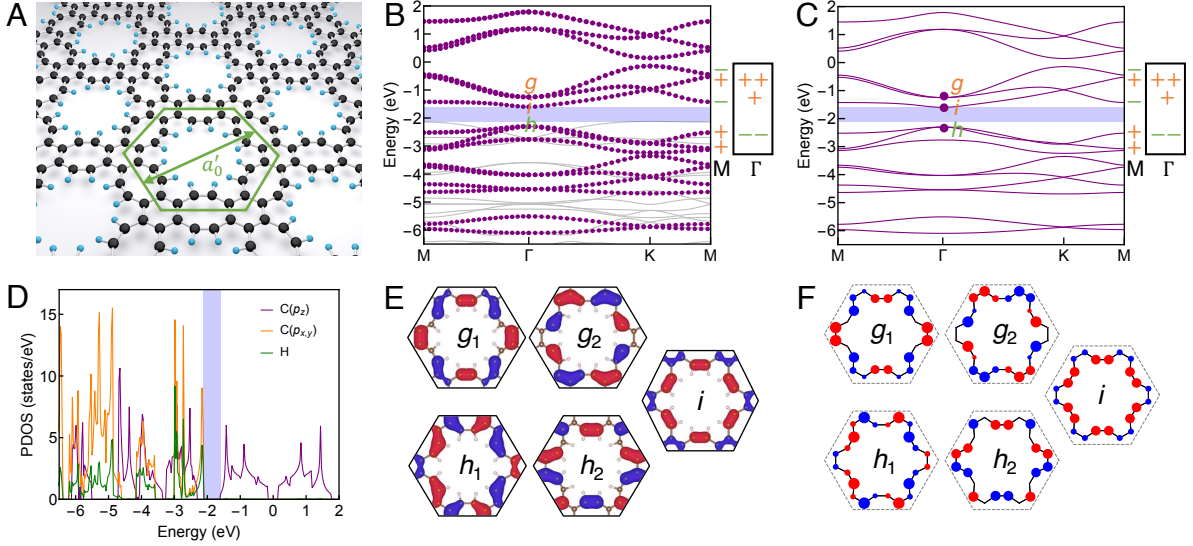


Figure 3. Hydrogenated holey graphyne (HHGY) and its band structures. (A) Stable structure of HHGY with lattice constant a'_0 obtained by DFT calculations, where carbon and hydrogen atoms are colored in black and cyan, respectively. The unit cell with the highest symmetry is denoted by a hexagon. (B) Band structures obtained by DFT calculations, with eigenstates projected to p_z orbitals and the bandgap shown by a region highlighted in blue. The g -, i - and h -like modes are labeled explicitly, and the parity of the eigenstates at Γ and M points for the corresponding five bands are denoted by plus and minus signs. (C) Same as (B) except for Wannier interpolation which is performed by projecting onto p_z orbitals on each carbon atom. (D) Projected density of states (PDOS) obtained by DFT calculations, with the bandgap shown by a region highlighted in blue. (E) Wave functions of g -, h - and i -like modes at the Γ point obtained by DFT calculations, with red/blue color denotes the plus/minus value. Notation: $g_1 \equiv g_{x^4-6x^2y^2+y^4}$, $g_2 \equiv g_{xy(x^2-y^2)}$, $h_1 \equiv h_{x(x^4-10x^2y^2+5y^4)}$, $h_2 \equiv h_{y(5x^4-10x^2y^2+y^4)}$, $i \equiv i_{x^6-15x^4y^2+15x^2y^4-y^6}$. (F) Same as (E) except for Wannier interpolation, with amplitude represented by size of dots.

by a band inversion between g - and h -like modes around the bandgap at the Γ point. As illustrated in Figures 3E and 3F, the eigenstates g -, h - and i -like modes are named by counting the number of nodes along the perimeter of hexagonal unit cell, i.e., 8, 10, and 12, with even, odd and even parity, respectively. Note that if the green hexagonal cell in Figure 3A is isolated and the hoppings between p_z orbitals are uniform, the classification by the number of nodes is exact and the eigenenergy should increase with the number of nodes. However, in Figure 3B, g -like mode comes above h -like mode, signaling a band inversion. For the two isolated valence p_z bands with h -like mode with odd parity at the Γ point and parity-even states at the M point, we evaluate the Wilson loop^{7,8} and find a phase winding of 2π , which indicates a nontrivial band topology (see Supporting Note S4).

Coming back to the full argument with the actual crystalline symmetry, doubly degenerate g - and h -like modes are the 2D irreducible representations of the C_{6v} symmetry in the material, while the singlet i -like mode is the 1D irreducible representation. With the double degeneracy, we can construct pseudospin states using g - and h -like modes:

$$|g_{\pm}\rangle = \frac{1}{\sqrt{2}} (|g_1\rangle \pm i |g_2\rangle), \quad |h_{\pm}\rangle = \frac{1}{\sqrt{2}} (|h_1\rangle \pm i |h_2\rangle). \quad (4)$$

We regard $|g_+\rangle$ and $|h_+\rangle$ as pseudospin-up states, since their phases of wave functions increase $+8\pi$ and $+10\pi$ counterclockwise along the perimeter of hexagonal unit cell, which correspond to the states with OAM $+4\hbar$ and $+5\hbar$, respectively, noting that the operator of OAM is $-i\hbar\frac{\partial}{\partial\phi}$. The time-reversal counterparts $|g_-\rangle$ and $|h_-\rangle$ are regarded as pseudospin-down states with OAM $-4\hbar$ and $-5\hbar$, respectively. Again, this argument is exact in the case of an isolated cell with a uniform hopping. In this system where there is only C_{6v} symmetry, the eigenstates are classified by OAM upto mod $6\hbar$, and $\pm 4\hbar$ and $\pm 5\hbar$ correspond to $\mp 2\hbar$ and $\mp \hbar$, respectively.

The nontrivial topology characterized by the \mathbb{Z}_2 topological index will manifest topological edge states. As can be seen in Figure 4A obtained by the Wannier TB calculations

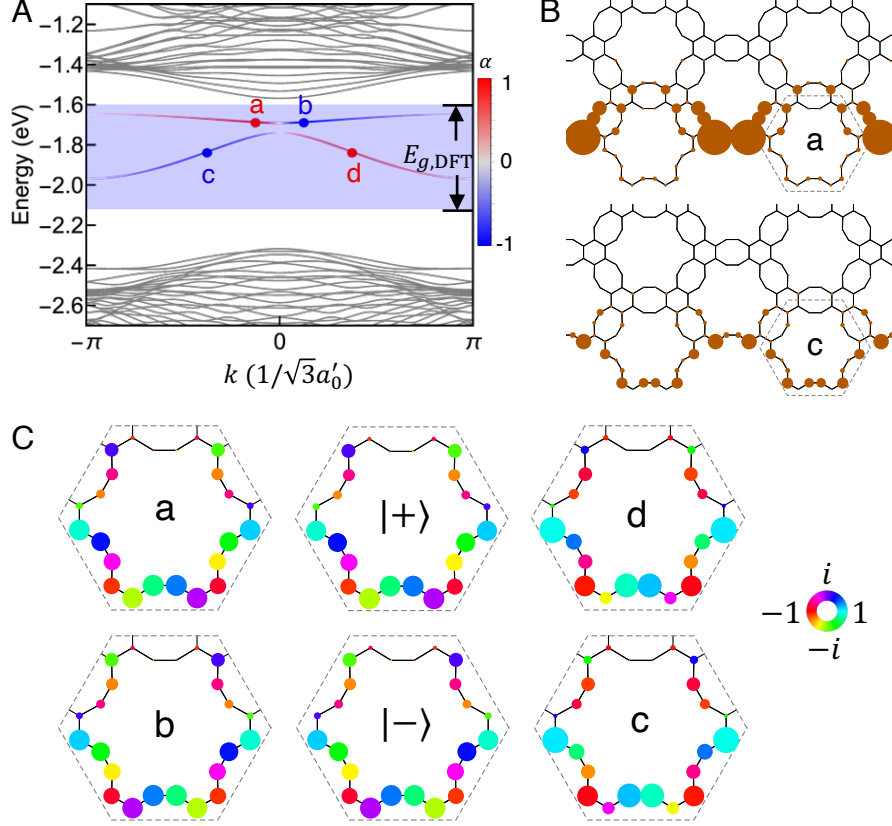


Figure 4. Topological edge states in a ribbon of HHGY. (A) Energy dispersion of a ribbon of HHGY obtained by Wannier TB calculations on p_z orbitals. The region highlighted in blue represents the DFT bulk bandgap, where the edge states are colored by their pseudospin polarizations α (see Supporting Note S5). (B) LDOS $|\psi_i|^2$ for the edge state “a” (upper panel) and “c” (lower panel) as labeled in (A), with the outmost unit cell highlighted by a dashed hexagon. (C) Comparison between the bulk pseudospin states $|\pm\rangle$ and the wave functions with spinful parts in the outmost unit cell of the four edge states “a” to “d”, with amplitude and phase denoted by size and color of dots, respectively.

on the ribbon structure where the hexagonal unit cells remain intact (see Supporting Note S1), a pair of topological edge states carrying opposite pseudospins appear within the DFT bulk bandgap (see Supporting Notes S5 for details). The LDOS of edge states are shown in Figure 4B (for detailed understanding see Supporting Notes S6), and the wave functions including phases with comparison to the bulk pseudospin states $|\pm\rangle$ ($= (|g_{\pm}\rangle \pm i|h_{\pm}\rangle)/\sqrt{2}$) are shown in Figure 4C.

It should be noted that although the edge morphology exhibiting the topological edge states in this work cannot be achieved by the available precursor directly, and thus trials on

edge treatments are required, such as out-of-plane hydrogenation.

In summary, we uncover topological electronic states in holey graphyne, through DFT calculations and Wannier TB modeling. Firstly, a nontrivial \mathbb{Z}_2 higher-order topological invariant is obtained arising from the C_2 symmetry of the material. We display explicitly the minimal nanoflakes hosting the corresponding corner states, which can be fabricated using the same precursor in the experiment,⁵ and the corner modes are ready to be observed by measuring differential conductance maps using STM. While so far the observation of topological corner modes in electronic systems has been limited to artificial lattices made by positioning carbon-monoxide molecules on Cu(111) surface,²⁹ holey graphyne could be the non-artificial material where topological electronic corner modes are experimentally observed. Secondly, by introducing an in-plane hydrogenation, holey graphyne opens a large energy gap of 0.52 eV at -2 eV, with a nontrivial topology arising from the band inversion between g - and h -like modes and characterized by a \mathbb{Z}_2 invariant. Topological edge states carrying opposite OAMs propagate in opposite directions, indicating potential applications in orbitronic devices with low energy loss workable at room temperature. Our work points out that holey graphyne serves as an ideal platform to observe topological electronic corner modes and edge states with OAMs protected by a large energy gap, opening a new avenue for further investigation and exploitation of topology in 2D carbon allotropes for both scientific understanding and practical applications.

Supporting Information Available

The Supporting Information is available free of charge at (website)

Section S1 on first-principles calculations and Wannier localization procedures; Section S2 on energy spectra and corner states of various HGY nanoflakes; Section S3 on adiabatic deformation of Wannier TB models between HGY and HHGY; Section S4 on Wilson loop calculations on HHGY; Section S5 on weights

of spinful and spinless parts for the wave functions of edge states in the HHGY ribbon; Section S6 on analysis on the wave functions of edge states in the HHGY ribbon (PDF)

Declaration of interests

The authors declare no competing financial interests.

Acknowledgement

This work is supported by CREST, JST (Core Research for Evolutionary Science and Technology, Japan Science and Technology Agency) (Grant Number JPMJCR18T4).

References

- (1) Haldane, F. D. M. Model for a Quantum Hall Effect without Landau Levels: Condensed-Matter Realization of the "Parity Anomaly". *Phys. Rev. Lett.* **1988**, *61*, 2015–2018.
- (2) Castro Neto, A. H.; Guinea, F.; Peres, N. M. R.; Novoselov, K. S.; Geim, A. K. The Electronic Properties of Graphene. *Rev. Mod. Phys.* **2009**, *81*, 109–162.
- (3) Kane, C. L.; Mele, E. J. Z_2 Topological Order and the Quantum Spin Hall Effect. *Phys. Rev. Lett.* **2005**, *95*, 146802.
- (4) Kane, C. L.; Mele, E. J. Quantum Spin Hall Effect in Graphene. *Phys. Rev. Lett.* **2005**, *95*, 226801.
- (14) Bernevig, B. A.; Hughes, T. L.; Zhang, S.-C. Quantum Spin Hall Effect and Topological Phase Transition in HgTe Quantum Wells. *Science* **2006**, *314*, 1757–1761.

- (6) Reis, F.; Li, G.; Dudy, L.; Bauernfeind, M.; Glass, S.; Hanke, W.; Thomale, R.; Schäfer, J.; Claessen, R. Bismuthene on a SiC Substrate: A Candidate for a High-Temperature Quantum Spin Hall Material. *Science* **2017**, *357*, 287–290.
- (7) Wu, S.; Fatemi, V.; Gibson, Q. D.; Watanabe, K.; Taniguchi, T.; Cava, R. J.; Jarillo-Herrero, P. Observation of the Quantum Spin Hall Effect up to 100 Kelvin in a Monolayer Crystal. *Science* **2018**, *359*, 76–79.
- (8) Deng, J.; Xia, B.; Ma, X.; Chen, H.; Shan, H.; Zhai, X.; Li, B.; Zhao, A.; Xu, Y.; Duan, W.; Zhang, S.-C.; Wang, B.; Hou, J. G. Epitaxial Growth of Ultraflat Stanene with Topological Band Inversion. *Nat. Mater.* **2018**, *17*, 1081–1086.
- (9) Collins, J. L.; Tadich, A.; Wu, W.; Gomes, L. C.; Rodrigues, J. N. B.; Liu, C.; Hellstedt, J.; Ryu, H.; Tang, S.; Mo, S.-K.; Adam, S.; Yang, S. A.; Fuhrer, M. S.; Edmonds, M. T. Electric-Field-Tuned Topological Phase Transition in Ultrathin Na₃Bi. *Nature* **2018**, *564*, 390–394.
- (10) Tang, S. et al. Quantum Spin Hall State in Monolayer 1T'-WTe₂. *Nat. Phys.* **2017**, *13*, 683–687.
- (11) Wu, L.-H.; Hu, X. Scheme for Achieving a Topological Photonic Crystal by Using Dielectric Material. *Phys. Rev. Lett.* **2015**, *114*, 223901.
- (12) Wu, L.-H.; Hu, X. Topological Properties of Electrons in Honeycomb Lattice with Detuned Hopping Energy. *Sci. Rep.* **2016**, *6*, 24347.
- (13) Kariyado, T.; Hu, X. Topological States Characterized by Mirror Winding Numbers in Graphene with Bond Modulation. *Sci. Rep.* **2017**, *7*, 16515.
- (14) Yang, Y.; Xu, Y. F.; Xu, T.; Wang, H.-X.; Jiang, J.-H.; Hu, X.; Hang, Z. H. Visualization of a Unidirectional Electromagnetic Waveguide Using Topological Photonic Crystals Made of Dielectric Materials. *Phys. Rev. Lett.* **2018**, *120*, 217401.

- (15) Li, Y.; Sun, Y.; Zhu, W.; Guo, Z.; Jiang, J.; Kariyado, T.; Chen, H.; Hu, X. Topological LC-circuits Based on Microstrips and Observation of Electromagnetic Modes with Orbital Angular Momentum. *Nat. Commun.* **2018**, *9*, 4598.
- (16) Barik, S.; Karasahin, A.; Flower, C.; Cai, T.; Miyake, H.; DeGottardi, W.; Hafezi, M.; Waks, E. A Topological Quantum Optics Interface. *Science* **2018**, *359*, 666–668.
- (17) Parappurath, N.; Alpegiani, F.; Kuipers, L.; Verhagen, E. Direct Observation of Topological Edge States in Silicon Photonic Crystals: Spin, Dispersion, and Chiral Routing. *Sci. Adv.* **2020**, *6*, eaaw4137.
- (18) Wang, X.-X.; Guo, Z.; Song, J.; Jiang, H.; Chen, H.; Hu, X. Unique Huygens-Fresnel Electromagnetic Transportation of Chiral Dirac Wavelet in Topological Photonic Crystal. *Nat. Commun.* **2023**, *14*, 3040.
- (19) Freeney, S. E.; van den Broeke, J. J.; Harsveld van der Veen, A. J. J.; Swart, I.; Morais Smith, C. Edge-Dependent Topology in Kekulé Lattices. *Phys. Rev. Lett.* **2020**, *124*, 236404.
- (20) Gomes, K. K.; Mar, W.; Ko, W.; Guinea, F.; Manoharan, H. C. Designer Dirac Fermions and Topological Phases in Molecular Graphene. *Nature* **2012**, *483*, 306–310.
- (21) Polini, M.; Guinea, F.; Lewenstein, M.; Manoharan, H. C.; Pellegrini, V. Artificial Honeycomb Lattices for Electrons, Atoms and Photons. *Nat. Nanotechnol.* **2013**, *8*, 625–633.
- (22) Benalcazar, W. A.; Bernevig, B. A.; Hughes, T. L. Quantized Electric Multipole Insulators. *Science* **2017**, *357*, 61–66.
- (23) Noh, J.; Benalcazar, W. A.; Huang, S.; Collins, M. J.; Chen, K. P.; Hughes, T. L.; Rechtsman, M. C. Topological Protection of Photonic Mid-Gap Defect Modes. *Nat. Photonics* **2018**, *12*, 408–415.

- (24) Serra-Garcia, M.; Peri, V.; Süsstrunk, R.; Bilal, O. R.; Larsen, T.; Villanueva, L. G.; Huber, S. D. Observation of a Phononic Quadrupole Topological Insulator. *Nature* **2018**, *555*, 342–345.
- (25) Peterson, C. W.; Benalcazar, W. A.; Hughes, T. L.; Bahl, G. A Quantized Microwave Quadrupole Insulator with Topologically Protected Corner States. *Nature* **2018**, *555*, 346–350.
- (26) Imhof, S.; Berger, C.; Bayer, F.; Brehm, J.; Molenkamp, L. W.; Kiessling, T.; Schindler, F.; Lee, C. H.; Greiter, M.; Neupert, T.; Thomale, R. Topoelectrical-Circuit Realization of Topological Corner Modes. *Nat. Phys.* **2018**, *14*, 925–929.
- (27) Xue, H.; Yang, Y.; Gao, F.; Chong, Y.; Zhang, B. Acoustic Higher-Order Topological Insulator on a Kagome Lattice. *Nat. Mater.* **2019**, *18*, 108–112.
- (28) Mittal, S.; Orre, V. V.; Zhu, G.; Gorlach, M. A.; Poddubny, A.; Hafezi, M. Photonic Quadrupole Topological Phases. *Nat. Photonics* **2019**, *13*, 692–696.
- (29) Kempkes, S. N.; Slot, M. R.; van den Broeke, J. J.; Capiod, P.; Benalcazar, W. A.; Vanmaekelbergh, D.; Bercioux, D.; Swart, I.; Morais Smith, C. Robust Zero-Energy Modes in an Electronic Higher-Order Topological Insulator. *Nat. Mater.* **2019**, *18*, 1292–1297.
- (12) Kariyado, T.; Jiang, Y.-C.; Yang, H.; Hu, X. Counterpropagating Topological Interface States in Graphene Patchwork Structures with Regular Arrays of Nanoholes. *Phys. Rev. B* **2018**, *98*, 195416.
- (31) Cai, J.; Ruffieux, P.; Jaafar, R.; Bieri, M.; Braun, T.; Blankenburg, S.; Muoth, M.; Seitsonen, A. P.; Saleh, M.; Feng, X.; Müllen, K.; Fasel, R. Atomically Precise Bottom-up Fabrication of Graphene Nanoribbons. *Nature* **2010**, *466*, 470–473.

- (32) Moreno, C.; Vilas-Varela, M.; Kretz, B.; Garcia-Lekue, A.; Costache, M. V.; Paradinas, M.; Panighel, M.; Ceballos, G.; Valenzuela, S. O.; Peña, D.; Mugarza, A. Bottom-up Synthesis of Multifunctional Nanoporous Graphene. *Science* **2018**, *360*, 199–203.
- (33) Haley, M. M. Synthesis and Properties of Annulenic Subunits of Graphyne and Graphdiyne Nanoarchitectures. *Pure Appl. Chem.* **2008**, *80*, 519–532.
- (34) Hu, Y.; Wu, C.; Pan, Q.; Jin, Y.; Lyu, R.; Martinez, V.; Huang, S.; Wu, J.; Wayment, L. J.; Clark, N. A.; Raschke, M. B.; Zhao, Y.; Zhang, W. Synthesis of γ -Graphyne Using Dynamic Covalent Chemistry. *Nat. Synth* **2022**, *1*, 449–454.
- (35) Son, Y.-W.; Cohen, M. L.; Louie, S. G. Half-Metallic Graphene Nanoribbons. *Nature* **2006**, *444*, 347–349.
- (36) Son, Y.-W.; Cohen, M. L.; Louie, S. G. Energy Gaps in Graphene Nanoribbons. *Phys. Rev. Lett.* **2006**, *97*, 216803.
- (37) Pan, L. D.; Zhang, L. Z.; Song, B. Q.; Du, S. X.; Gao, H.-J. Graphyne- and Graphdiyne-Based Nanoribbons: Density Functional Theory Calculations of Electronic Structures. *Appl. Phys. Lett.* **2011**, *98*, 173102.
- (38) Liu, B.; Zhao, G.; Liu, Z.; Wang, Z. F. Two-Dimensional Quadrupole Topological Insulator in γ -Graphyne. *Nano Lett.* **2019**, *19*, 6492–6497.
- (39) Cranford, S. W.; Buehler, M. J. Mechanical Properties of Graphyne. *Carbon* **2011**, *49*, 4111–4121.
- (5) Liu, X.; Cho, S. M.; Lin, S.; Chen, Z.; Choi, W.; Kim, Y.-M.; Yun, E.; Baek, E. H.; Ryu, D. H.; Lee, H. Constructing Two-Dimensional Holey Graphyne with Unusual Annulative π -Extension. *Matter* **2022**, *5*, 2306–2318.
- (41) Marzari, N.; Mostofi, A. A.; Yates, J. R.; Souza, I.; Vanderbilt, D. Maximally Localized Wannier Functions: Theory and Applications. *Rev. Mod. Phys.* **2012**, *84*, 1419–1475.

- (42) Mizoguchi, T.; Araki, H.; Hatsugai, Y. Higher-Order Topological Phase in a Honeycomb-Lattice Model with Anti-Kekulé Distortion. *J. Phys. Soc. Jpn.* **2019**, *88*, 104703.
- (43) Kudo, K.; Yoshida, T.; Hatsugai, Y. Higher-Order Topological Mott Insulators. *Phys. Rev. Lett.* **2019**, *123*, 196402.
- (44) Araki, H.; Mizoguchi, T.; Hatsugai, Y. \mathbb{Z}_Q Berry Phase for Higher-Order Symmetry-Protected Topological Phases. *Phys. Rev. Res.* **2020**, *2*, 012009.
- (45) Benalcazar, W. A.; Teo, J. C. Y.; Hughes, T. L. Classification of Two-Dimensional Topological Crystalline Superconductors and Majorana Bound States at Disclinations. *Phys. Rev. B* **2014**, *89*, 224503.
- (7) Yu, R.; Qi, X. L.; Bernevig, A.; Fang, Z.; Dai, X. Equivalent Expression of Z_2 Topological Invariant for Band Insulators Using the Non-Abelian Berry Connection. *Phys. Rev. B* **2011**, *84*, 75119.
- (8) Weng, H.; Yu, R.; Hu, X.; Dai, X.; Fang, Z. Quantum Anomalous Hall Effect and Related Topological Electronic States. *Adv. Phys.* **2015**, *64*, 227–282.

Supporting Information for Topological electronic states in holey graphyne

1 First-principles calculations and Wannier localization procedures

First-principles calculations are performed within the DFT scheme using the Vienna *Ab initio* Simulation Package,^{S1} where the projector augmented-wave method,^{S2} the Perdew-Becke-Erzenhof type generalized gradient approximation^{S3} for the exchange-correlation potential and a plane-wave basis set with a cutoff energy of 520 eV are adopted. A $11 \times 11 \times 1$ k -point mesh is used for both structure relaxations and self-consistent calculations. The structure relaxations are performed until the Hellmann-Feynman forces acting on ions are smaller than 10^{-4} eV/Å and the energy tolerances are below 10^{-6} eV/atom. Graphyne sheets are separated by a vacuum layer of 2 nm, ensuring that interlayer couplings are negligible. The data post-processing is done using VASPKIT.^{S4}

In Figure S1A we give the bond lengths and angles obtained by the ion relaxation in DFT calculations for HGY, which successfully reproduces the bonding information in Ref. S5. With the C_{6v} symmetry of HGY, the shown information fixes the crystalline structure completely, namely we can derive all other bond lengths and angles. The lattice constant is $a_0 = 10.85$ Å, which has already been given in the main text. For HHGY, the bond lengths and angles are given in Figure S1B, with the lattice constant $a'_0 = 11.02$ Å.

MLWF are obtained from data in first-principles calculations using WANNIER90.^{S6} For HGY, the Wannier localization procedures are performed by projecting the eigenstates onto p_z orbitals on each atom and p_{\parallel} orbitals on atoms C'. The outer energy window is set as $E_{\text{out}} \in [-7 \text{ eV}, 12 \text{ eV}]$ to include all p orbitals, and the frozen energy window is set as $E_{\text{froz}} \in [-5.3 \text{ eV}, 2.4 \text{ eV}]$.

For HHGY, the projection orbitals are p_z orbitals on each carbon atom and bonding sp orbitals at the centers of C-H bonds. The outer energy window is the same as the case for HGY, while the frozen energy window starts from -4.5 eV to avoid other orbitals. We show

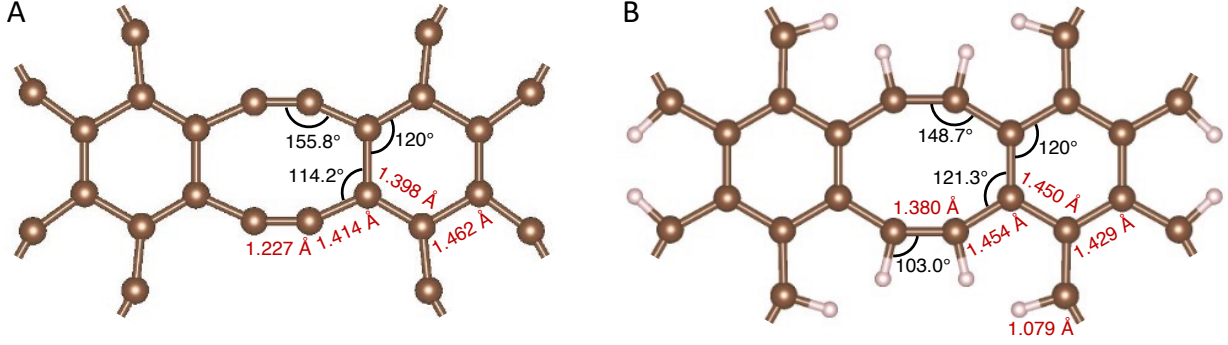


Figure S1. Bonding information. (A) Bond lengths and angles of HGy obtained by DFT calculations. (B) Same as (A) except for HHGy.

only the interpolated band structure for p_z orbitals in Figure 3C in the main text, since the sp orbitals are orthogonal to the p_z orbitals and irrelevant for our discussion.

In the calculation of the HOT index γ for HGy, a pair of twist phases θ are introduced in a supercell consisting of 3×3 rhombic unit cells with periodic boundary conditions applied in two in-plane directions. For the ribbon structure of HHGy, the calculation is performed on a supercell composed of 20 hexagonal unit cells using a Wannier TB Hamiltonian.

2 Energy spectra and corner states of various HGy nanoflakes

For the nanoflakes with one and two rhombic unit cells, the bulk and corner are not well-defined, and thus we start with nanoflakes with three rhombic unit cells, where there are three different configurations as shown in Figure S2. In Figure S2A we display the energy spectrum for the straight type, and find two in-gap states of p_z orbital. These two in-gap states possess even and odd parity with respect to the center of nanoflake, which correspond to the bonding and antibonding states, respectively, as shown in Figure S2A. Although these two states originate from the nontrivial HOT in this nanoflake with two corners, only the antibonding state can be regarded as a corner state, while it is not the case for the bonding state which has strong overlap at the central unit cell. The energy of the antibonding state is -1.85 eV, and the energetically closest state is the bulk state of $p_{||}$ orbital at -1.93 eV. The

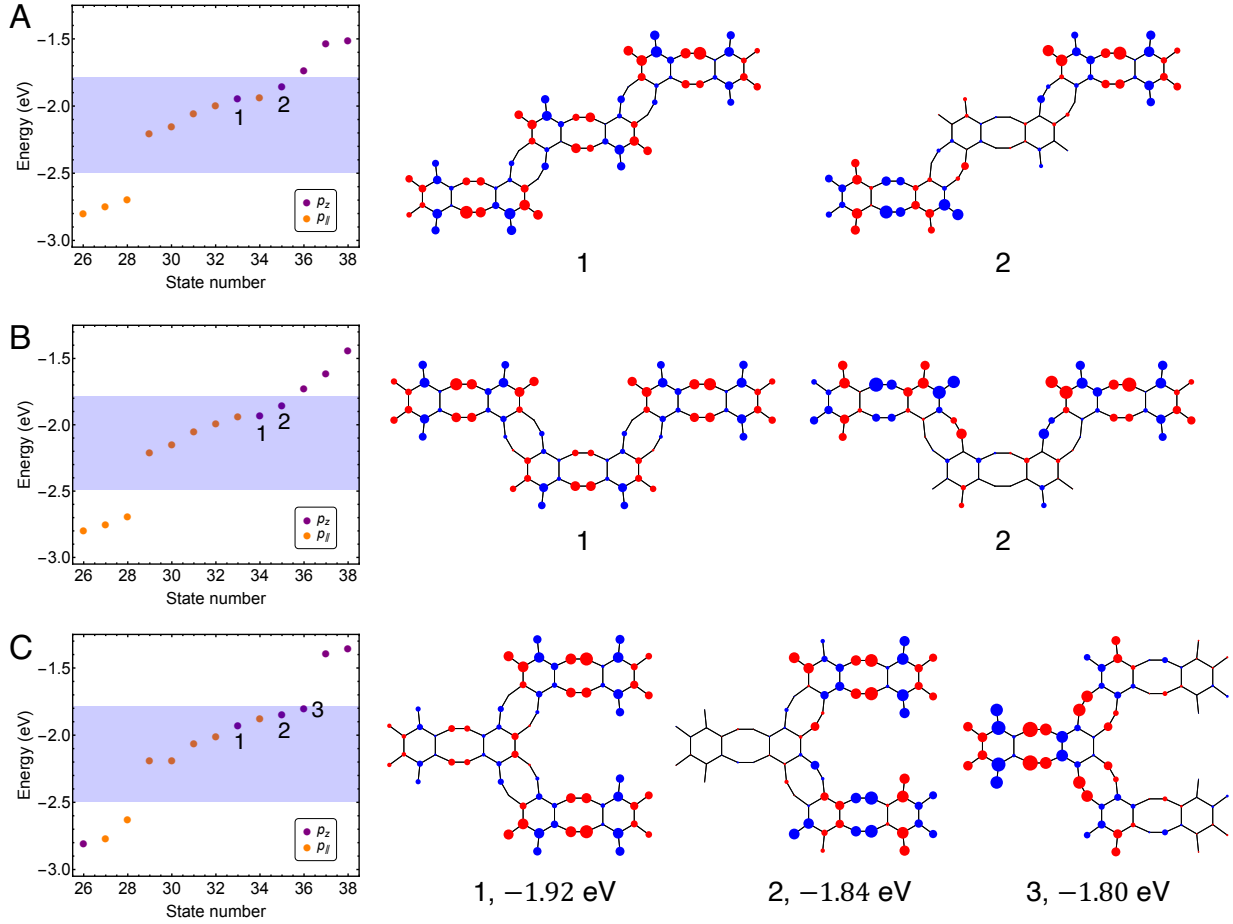


Figure S2. Energy spectra and corner modes of HGY nanoflakes with three rhombic unit cells. (A) (left panel) Energy spectrum for straight type with corner states labeled by numbers. The region highlighted in blue represents the bulk bandgap of p_z orbitals shown in Figure 3C in the main text. (right panel) Wave functions of corner modes with amplitude represented by dot size and positive/negative signs in red/blue. (B and C) Same as (A) except for boomerang type-I (B) and type-II (C).

energy difference of 0.08 eV is enough for STM technique to detect the antibonding state. Therefore, the nanoflake with three rhombic unit cells is the minimal one hosting topological corner modes which can be detected experimentally.

For the boomerang type-I shown in Figure S2B, similar to the straight type discussed in the previous paragraph, there are bonding (mirror-even) and antibonding (mirror-odd) states in the energy gap, and only the latter one can be regarded as a corner state (here, the mirror plane is vertical in the figure). The energy of the antibonding state is -1.85 eV,

and the energetically closest state is the bonding state at -1.93 eV. The energy difference of 0.08 eV is enough for STM technique to detect this antibonding state.

For the boomerang type-II shown in Figure S2C, different from the two previous cases, there are three in-gap states because this nanoflake has three corners. States 1 and 2 with energy of -1.92 eV and -1.84 eV respectively are the bonding (mirror-even) and antibonding (mirror-odd) states localized at the upper and lower corners, while state 3 with energy of -1.80 eV is a mirror-even state localized at the central corner (here, the mirror plane is horizontal in the figure). All these three in-gap states can be regarded as corner states from their wave functions (see LDOS in Figure 2 in the main text for a clearer visualization). The energetically closest bulk state is at -1.87 eV, meaning that the smallest energy gap between the corner states and bulk states is 0.03 eV, still large enough for STM technique to detect all the three corner states.

In order to show that the in-gap states are second-order topological corner states instead of first-order topological end states, we perform calculations on nanoflakes with larger sizes. In Figure S3A we show a nanoflake with five rhombic unit cells, which has the highest symmetry, namely, mirror symmetry along both horizontal and vertical directions. Four corner states, s , p_x , d_{xy} and p_y modes, appear within the energy gap, corresponding to state 1 to 4 in Figure S3A respectively, with slightly different energies due to the coupling between corner states. Increasing the number of unit cells to 13, it is clear that the four states in the nanoflake demonstrate strong localization at the corners within the outmost unit cells, not along the edge, as shown in Figure S3B. It is not difficult to imagine that, when the flake is large enough so that the coupling between two corners becomes negligible, the two mirror symmetries guarantee four-fold degenerate states with each localized at one of the four corners. Comparing the wave functions at the upper-right corner in all the corner states shown in Figures S2 and S3 (except for state 3 in Figure S2C where the wave function localizes at the left corner), we can see that they all look similar, indicating that they originate from the same HOT. Therefore, the nanoflakes with three rhombic unit cells

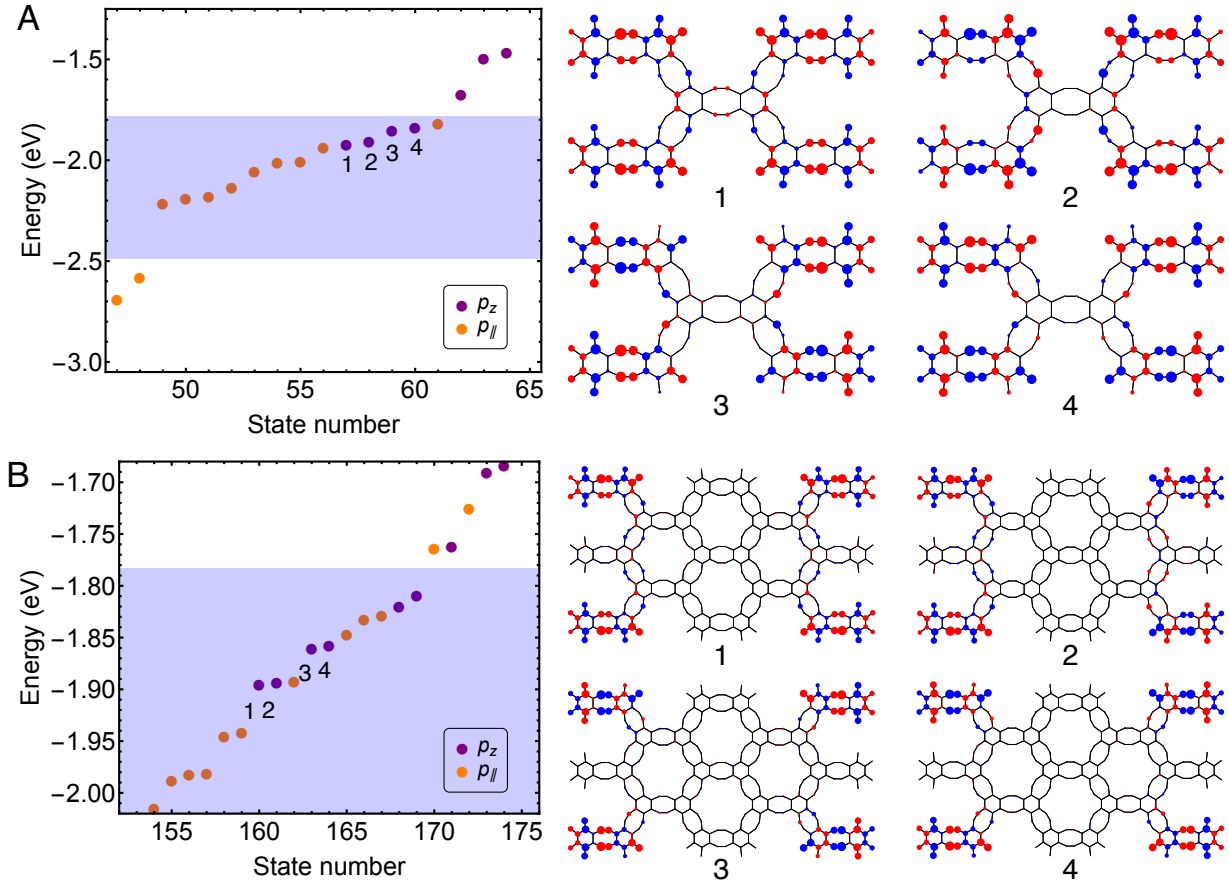


Figure S3. Energy spectra and corner modes of larger HGY nanoflakes. (A) (left panel) Energy spectrum for the nanoflake with five rhombic unit cells. The corner states are labeled by numbers, and the region highlighted in blue represents the bulk bandgap of p_z orbitals shown in Figure 3C in the main text. (right panel) Wave functions of corner modes with amplitude represented by dot size and positive/negative signs in red/blue. (B) Same as (A) except for a nanoflake with 13 unit cells.

are the minimal ones which host topological corner states detectable experimentally.

In principle, $p_{||}$ orbitals could also host HOTI states. However, the corresponding energy gaps are too small for experimental observations.

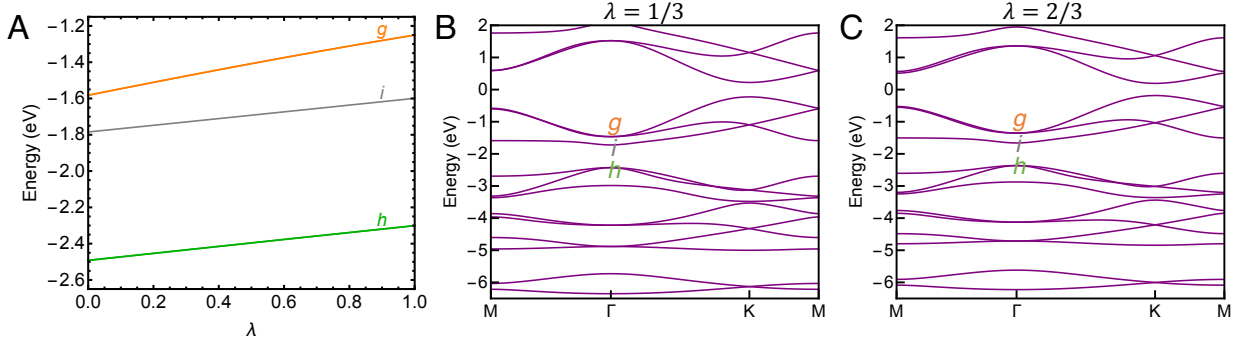


Figure S4. Adiabatic deformation of Wannier TB models between HGY and HHGY. (A) λ dependence of energies of g -, h - and i -like modes in adiabatic deformation on hoppings with λ defined in Equation (S1). No energy crossing occurs in these three modes. (B and C) Band structures with hoppings given by $\lambda = 1/3$ and $\lambda = 2/3$. h -like modes are at the top of the valence bands and i -like mode is at the bottom of the conduction band.

3 Adiabatic deformation of Wannier TB models between HGY and HHGY

In the main text, we have seen that HGY and HHGY share the same parity index (N_{Γ}^+ , N_M^+) for the p_z bands. In order to confirm that these two phases are the same in topology, we consider a continuous transformation between the effective models for HGY and HHGY. For this purpose, the TB models derived using the MLWF method are utilized,

$$H_{\lambda}(\mathbf{k}) = (1 - \lambda)H_{\text{HGY}}^{\text{TB}}(\mathbf{k}) + \lambda H_{\text{HHGY}}^{\text{TB}}(\mathbf{k}), \quad (\text{S1})$$

where $H_{\text{HGY}}^{\text{TB}}(\mathbf{k})$ and $H_{\text{HHGY}}^{\text{TB}}(\mathbf{k})$ are the TB Hamiltonians for HGY and HHGY, respectively. This interpolation is possible since $H_{\text{HGY}}^{\text{TB}}(\mathbf{k})$ and $H_{\text{HHGY}}^{\text{TB}}(\mathbf{k})$ have the same size as far as the p_z bands are concerned. The band edge energies (at the Γ point) as a function of λ are shown in Figure S4A, where there is no band crossing. Therefore, the electronic structures for HGY and HHGY are adiabatically connected without gap closing. As can be read from Figures S4B and S4C the electronic structures are also smoothly transformed from HGY to HHGY, preserving the target energy gap.

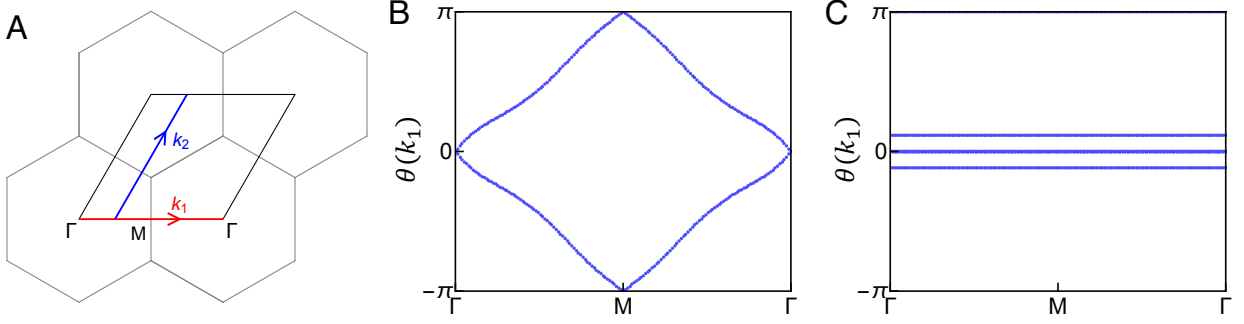


Figure S5. Wilson loop of HHGY. (A) Paths for calculations on Wilson loop. (B) Wilson loop spectrum along k_1 direction for the two isolated bands just below the energy gap at -2 eV shown in Figure 3C in the main text, which demonstrates a nontrivial \mathbb{Z}_2 topology. (C) Same as (B) except for all nine valence bands.

4 Wilson loop calculations on HHGY

The Wilson loop along the k_1 direction in the BZ in Figure S5A is given by^{S7,S8}

$$\mathcal{W}(k_1) = \mathcal{P} \exp \left[-i \oint_{k_2} dk_2 \mathcal{A}_1(k_1, k_2) \right], \quad (\text{S2})$$

where the path-ordered integration is at fixed k_1 with k_2 across the BZ (for example from $k_2 = 0$ to $k_2 = 2\pi$ as shown in Figure S5A), and $\mathcal{A}_1(k_1, k_2)$ is the Berry connection matrix along k_1 direction with the element defined as

$$\mathcal{A}_1^{mn}(k_1, k_2) = \langle u_m(k_1, k_2) | \partial_{k_1} | u_n(k_1, k_2) \rangle \quad (\text{S3})$$

with $|u_m(k_1, k_2)\rangle$ the eigenstate in the m -th band. The phase of eigenvalue of Wilson loop is

$$\theta(k_1) = \text{Im} [\ln \text{eig}(\mathcal{W}(k_1))]. \quad (\text{S4})$$

We calculate the phase of Wilson loop eigenvalue for the two isolated bands just below the energy gap at -2 eV in HHGY (see Figure 3C in the main text), where the Γ point is occupied by two degenerate h -like modes with odd parity whereas the M point is occupied by

two states with even parity. As displayed in Figure S5, taking the path $k_1 = 0 \rightarrow \pi \rightarrow 2\pi$, i.e., $\Gamma \rightarrow M \rightarrow \Gamma$, $\theta(k_1)$ has a phase winding of 2π , indicating the nontrivial band topology. With all nine valence bands taken into calculation, there is no phase winding in $\theta(k_1)$ as shown in Figure S5C, indicating a trivial topology. The phase winding situations in Figures S5B and S5C signal a fragile topology in the top two valence bands.^{S9,S10}

5 Weights of spinful and spinless parts for the wave functions of edge states in the HHGY ribbon

For the wave functions of edge states, we compare the weights between spinful parts from g - and h -like modes and the spinless part from the i -like mode, and find that the spinful parts predominate in these edge states (74~95% around $k = 0$, see Figures S6A). Therefore, we first focus on the spinful parts, and introduce a quantity to measure the polarization of pseudospin:

$$\alpha = \frac{|\langle +|\psi\rangle|^2 - |\langle -|\psi\rangle|^2}{|\langle +|\psi\rangle|^2 + |\langle -|\psi\rangle|^2}, \quad (\text{S5})$$

where $|\psi\rangle$ is the wave function in the outmost unit cell of ribbon, and $|\pm\rangle = (|g_{\pm}\rangle \pm i|h_{\pm}\rangle)/\sqrt{2}$ denoting the pseudospin-up/-down state in the hexagonal unit cell (see Refs. S11 and S12 for the analytical solutions of edge states $|p_{\pm}\rangle \pm i|d_{\pm}\rangle$, where a p - d band inversion occurs).

In Figures S6B, we display the pseudospin polarization α for the edge states as a function of Bloch momentum. In the upper energy dispersion, α remains positive for $k < 0$ while negative for $k > 0$, showing that the dispersion is divided into two parts, with the left/right one occupied by pseudospin-up/-down states. For edge state “a”, α reaches nearly unity at $k = -\pi/8$, indicating a well developed pseudospin-up characteristic, whereas edge state “b” at $k = \pi/8$, as the time-reversal counterpart for state “a”, exhibits a well developed pseudospin-down characteristic. Due to the absence of chiral symmetry, the degeneracy at $k = 0$ is lifted with a small energy gap, as compared with a large energy gap at $k = \pm\pi$, which leads to the two states $|g_1\rangle - |h_2\rangle$ (mirror-even) and $|g_2\rangle + |h_1\rangle$ (mirror-odd) with

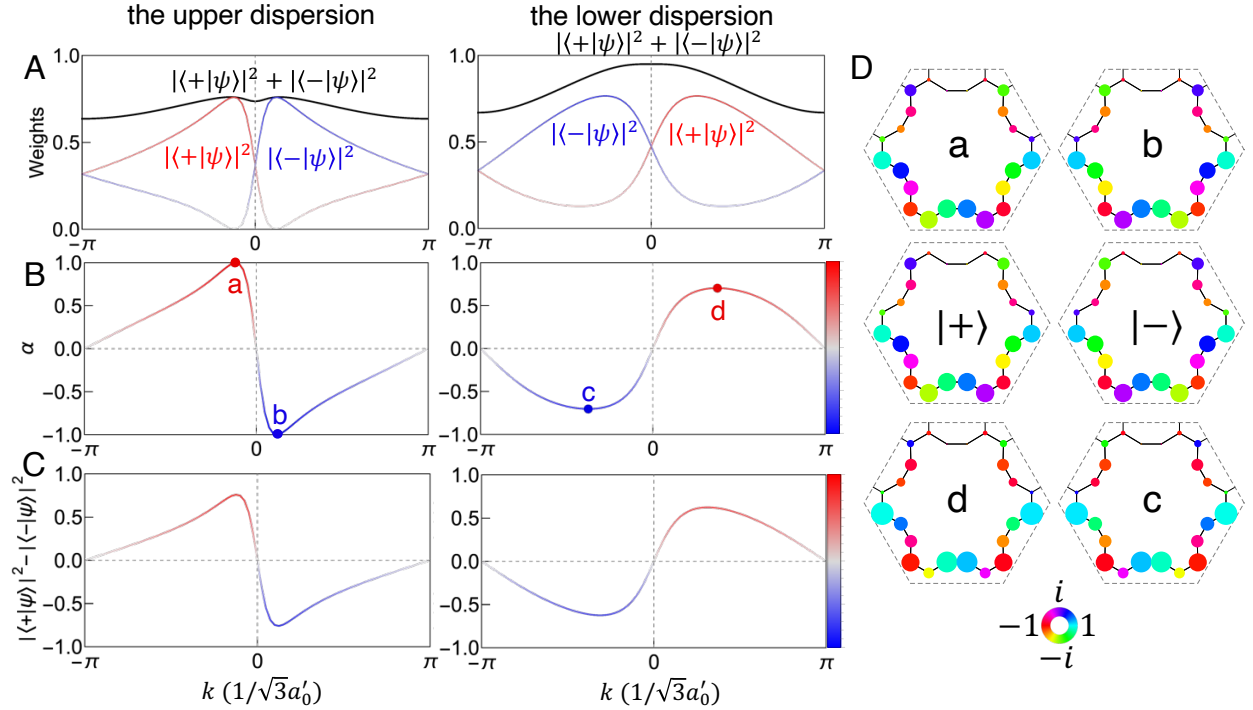


Figure S6. Weights of spinful parts for the wave functions of edge states in the ribbon of HHGY in Figure 4 in the main text. (A) Weights of pseudospin-up and -down parts for the wave functions of edge states in the upper and lower dispersions shown in Figure 4A in the main text. (B) Same as (A) except for α . (C) Same as (A) except for the weight difference between pseudospin-up and -down parts. (D) Reproduced from Figure 4C in the main text for convenience.

zero spin polarization at $k = 0$ (see Figure 3E in the main text and Figure S7A). In the simpler modulated honeycomb lattice model where the topological nontriviality is manifested by the band inversion between p - and d -modes, the chiral symmetry (sublattice symmetry) combined with the mirror symmetry is the key to suppress the minigap,^{S13} in contrast to the present system where the chiral symmetry is not active.

In the lower energy dispersion, the edge states for $k < 0$ ($k > 0$) are pseudospin-down (-up), which is opposite to the upper energy dispersion. Therefore, as depicted in Figure 4A in the main text, the edge states with opposite pseudospins counterpropagate on the same edge of ribbon, exhibiting the feature of pseudospin-momentum locking, reminiscent of QSHE.^{S14}

In Figure 4B in the main text, we plot the LDOS $|\psi_i|^2$ for edge state “a” and “c”, which demonstrate a strong localization on the edge. The LDOS for edge states “b” and “d” are identical to those for “a” and “c”, respectively, as guaranteed by TRS. We extract the wave functions with only spinful parts in the outmost unit cell, which is illustrated in Figure S6D, and compare them with the pseudospin-up state $|+\rangle$ and the pseudospin-down state $|-\rangle$. The wave functions for “a” and “b” show a perfect match to $|+\rangle$ and $|-\rangle$, respectively, which is consistent with the almost full pseudospin polarization. For wave functions “c” and “d”, there are slight deviations in amplitudes and phases, indicating a small mixing between the pseudospin-up and -down states. The time-reversal symmetry between states “a” and “b” (as well as “c” and “d”) is reflected in the opposite phases of their wave functions.

In Figure S6A, we display the weights of spinful parts for the wave functions of edge states in the HHGY ribbon shown in Figure 4 in the main text. For the wave functions of edge states in the upper dispersion, as shown in the left panel of Figure S6A, the weight of spinful parts $|\langle +|\psi\rangle|^2 + |\langle -|\psi\rangle|^2$ is 74% at $k = 0$ and has a maximum 76% at $k = 0.15\pi$. The rest is the spinless part, which comes from the i -like band. Although the edge states originate from the g - h band inversion, there is a moderate contribution from the i -like band, since it is the lowest conduction band around the Γ point lying between the g - and h -like bands and is close to the upper edge dispersion energetically (see Figures 3B and 4A in the

main text). For the wave functions of edge states in the lower dispersion, as shown in the right panel of Figure S6A, the weight of spinful parts is 90% \sim 95% within $k = \pm 0.3\pi$. For the wave functions in both the upper and lower edge dispersions, the spinful parts dominate around $k = 0$, which justifies the treatment in the main text where the spinful parts are focused.

In Equation S5 α is defined as the pseudospin polarization within spinful parts of wave function. When the spinless part of wave function is included, the polarization is the weight difference between pseudospin-up and -down parts of wave function. The polarizations for the upper and lower edge dispersions in Figure S6C have lower peak values of 0.76 and 0.62 as compared with 1.00 and 0.70 in α in Figure S6B, respectively. The difference is larger in the upper dispersion, because it is energetically closer to the i -like band.

6 Analysis on the wave functions of edge states in the HHGY ribbon

The edge wave functions corresponding to the LDOS in Figure 4C in the main text is shown in Figure S7A, where state “a” dominates on the concave region of edge, while state “c” dominates on the outmost carbon chain. The system can be modeled by a simple TB model with nearest-neighbor (NN) hopping called graphene with $2\sqrt{3} \times 2\sqrt{3}$ nanohole array as shown in Figure S7B (see Figure 1F in Ref. S12 for graphene with $4\sqrt{3} \times 4\sqrt{3}$ nanohole array), presuming that the NN hopping between two atoms C’ in HHGY shown in Figure 3A in the main text is large enough to treat them as a composite atom. The TB Hamiltonian is given by^{S12}

$$H = -t \sum_{\langle mn \rangle} c_m^\dagger c_n, \quad (\text{S6})$$

where only the NN hopping $t = -2.7$ eV is considered. The eigenstate of this Hamiltonian can be expressed using $|\psi_{0,1}, \psi_{0,2}, \dots, \psi_{i,j}, \dots, \psi_{N,18}\rangle$, where $\psi_{i,j}$ is the local wave function at site j in the i -th hexagonal unit cell. From the hexagonal unit cell shown in Figure S7C,

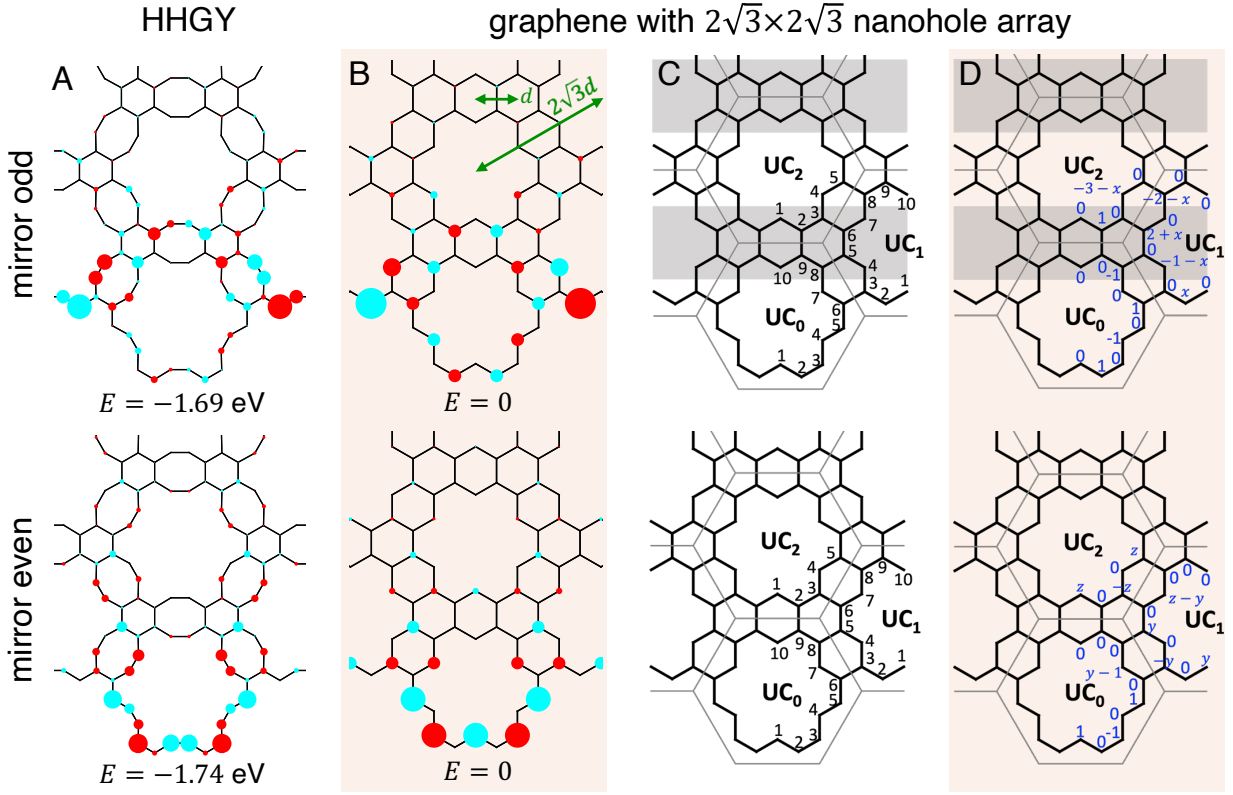


Figure S7. Solutions for edge states. (A) Wave functions of edge states in the HHGY ribbon with energies of -1.69 eV and -1.74 eV at $k = 0$ shown in Figure 4C in the main text obtained numerically using the Wannier TB model. Their mirror symmetries are odd and even, respectively. (B) Analytical solutions for zero-energy modes at $k = 0$ in a ribbon of graphene with $2\sqrt{3} \times 2\sqrt{3}$ nanohole array, where the lattice constant in bulk is $2\sqrt{3}d$ with d being the lattice constant of pristine graphene. (C) Schematic figures labeling the sites in three outmost unit cells on the edge, with the upper/lower one for the mirror-odd/even state. (D) Same as (C) except for analytical solutions of zero-energy modes. The values of x , y and z are derived in the text.

we can see that this system has chiral (sublattice) symmetry. With the Hamiltonian in Equation (S6), one can obtain the zero-energy edge modes at $k = 0$ in a ribbon structure shown in Figure S7B analytically with the help of the chiral symmetry and the mirror symmetry, as shown in what follows.

When the state at $k = 0$ is concerned, the ribbon can be treated as a cylinder with the diameter to be the lattice constant of supercell.^{S13} Take the upper panel of Figure S7C for example, the left and right sides are connected with each other, and the edge is of open boundary condition (the top edge is not shown in the figure). In order to obtain the

zero-energy mode with odd mirror symmetry, we use the upper panel of Figure S7C as the schematic figure for derivation of wave functions. With the mirror symmetry, we only need to consider the wave functions at ten sites in one unit cell. When the mirror symmetry is odd, the wave functions at site 1 and 10 are zero,

$$\psi_{i,1}^{\circ} = \psi_{i,10}^{\circ} = 0, \quad i \in N, \quad (\text{S7})$$

where the superscript “o” denotes odd mirror symmetry and i labels the unit cell. Setting $\psi_{0,2}^{\circ} = 1$ and considering the state is of zero energy, referring to site 2 in the 0th unit cell there is a relation: $\psi_{0,1}^{\circ} + \psi_{0,3}^{\circ} = 0$, giving

$$(\text{site } 0, 2) \quad \psi_{0,3}^{\circ} = -\psi_{0,1}^{\circ} = 0. \quad (\text{S8})$$

Similarly, we can obtain the relations for the following sites:

$$\begin{aligned} (\text{site } 0, 3) \quad \psi_{0,4}^{\circ} &= -\psi_{0,2}^{\circ} = -1, \\ (\text{site } 0, 4) \quad \psi_{0,5}^{\circ} &= -\psi_{0,3}^{\circ} = 0, \\ (\text{site } 0, 5) \quad \psi_{0,6}^{\circ} &= -\psi_{0,4}^{\circ} = 1, \\ (\text{site } 1, 2) \quad \psi_{1,3}^{\circ} &= -\psi_{1,1}^{\circ} = 0, \\ (\text{site } 0, 6) \quad \psi_{0,7}^{\circ} &= -\psi_{0,5}^{\circ} - \psi_{1,3}^{\circ} = 0. \end{aligned} \quad (\text{S9})$$

Set $\psi_{1,2}^{\circ} = x$ and the relations of wave functions at the following sites can be derived:

$$\begin{aligned}
(\text{site } 1, 3) \quad \psi_{1,4}^{\circ} &= -\psi_{0,6}^{\circ} - \psi_{1,2}^{\circ} = -1 - x, \\
(\text{site } 0, 7) \quad \psi_{0,8}^{\circ} &= -\psi_{0,6}^{\circ} = -1, \\
(\text{site } 1, 4) \quad \psi_{1,5}^{\circ} &= -\psi_{1,3}^{\circ} = 0, \\
(\text{site } 0, 8) \quad \psi_{0,9}^{\circ} &= -\psi_{0,7}^{\circ} - \psi_{1,5}^{\circ} = 0, \\
(\text{site } 1, 5) \quad \psi_{1,6}^{\circ} &= -\psi_{0,8}^{\circ} - \psi_{1,4}^{\circ} = 2 + x, \\
(\text{site } 0, 9) \quad \psi_{2,2}^{\circ} &= -\psi_{0,8}^{\circ} - \psi_{0,10}^{\circ} = 1, \\
(\text{site } 2, 2) \quad \psi_{2,3}^{\circ} &= -\psi_{0,9}^{\circ} - \psi_{2,1}^{\circ} = 0, \\
(\text{site } 1, 6) \quad \psi_{1,7}^{\circ} &= -\psi_{1,5}^{\circ} - \psi_{2,3}^{\circ} = 0,
\end{aligned} \tag{S10}$$

which are the wave functions in the gray region acrossing the 1st unit cell (see the upper panel of Figure S7C). Stepping further into the bulk, the wave functions in the white stripe region acrossing the 2nd unit cell should have similar relations as Equation (S10), since the gray region becomes the white region by shifting a unit vector considering the periodicity of the model away from the edge. Therefore, the wave functions for the stripe regions acrossing the i -th unit cell are:

$$\psi_{i,4}^{\circ} = -\psi_{i-1,6}^{\circ} - \psi_{i,2}^{\circ}, \tag{S11a}$$

$$\psi_{i-1,8}^{\circ} = -\psi_{i-1,6}^{\circ}, \tag{S11b}$$

$$\psi_{i,6}^{\circ} = -\psi_{i-1,8}^{\circ} - \psi_{i,4}^{\circ}, \tag{S11c}$$

$$\psi_{i+1,2}^{\circ} = -\psi_{i-1,8}^{\circ} - \psi_{i-1,10}^{\circ} = -\psi_{i-1,8}^{\circ}, \tag{S11d}$$

with $i \in N_+$, and the following wave functions are zero:

$$\psi_{i,j}^{\circ} = 0 \quad (i \in N, j = 1, 3, 5, 7, 9, 10). \tag{S12}$$

Equation (S11) can be reorganized to show the relations of wave functions between two neighboring unit cells. With Equations (S11a) \sim (S11c), we have

$$\begin{aligned}
\psi_{i,6}^{\circ} &= -\psi_{i-1,8}^{\circ} - \psi_{i,4}^{\circ} \\
&= \psi_{i-1,6}^{\circ} - \psi_{i,4}^{\circ} \\
&= -\psi_{i,2}^{\circ} - 2\psi_{i,4}^{\circ}.
\end{aligned} \tag{S13}$$

With Equations (S11a), (S11b) and (S11d), we have

$$\begin{aligned}
\psi_{i+1,2}^{\circ} &= -\psi_{i-1,8}^{\circ} \\
&= \psi_{i-1,6}^{\circ} \\
&= -\psi_{i,2}^{\circ} - \psi_{i,4}^{\circ}.
\end{aligned} \tag{S14}$$

With Equations (S11a), (S13) and (S14), we have

$$\begin{aligned}
\psi_{i+1,4}^{\circ} &= -\psi_{i-1,6}^{\circ} - \psi_{i+1,2}^{\circ} \\
&= (\psi_{i,2}^{\circ} + 2\psi_{i,4}^{\circ}) + (\psi_{i,2}^{\circ} + \psi_{i,4}^{\circ}) \\
&= 2\psi_{i,2}^{\circ} + 3\psi_{i,4}^{\circ}.
\end{aligned} \tag{S15}$$

With Equations (S13) \sim (S15), the nonzero wave functions in Equation (S11) can be rewritten as

$$\begin{pmatrix} \psi_{i+1,2}^{\circ} \\ \psi_{i+1,4}^{\circ} \end{pmatrix} = \begin{pmatrix} -1 & -1 \\ 2 & 3 \end{pmatrix} \begin{pmatrix} \psi_{i,2}^{\circ} \\ \psi_{i,4}^{\circ} \end{pmatrix}, \tag{S16a}$$

$$\psi_{i,6}^{\circ} = -\psi_{i,2}^{\circ} - 2\psi_{i,4}^{\circ}, \tag{S16b}$$

$$\psi_{i,8}^{\circ} = \psi_{i,2}^{\circ} + 2\psi_{i,4}^{\circ}, \tag{S16c}$$

for $i \in N_+$, where Equation (S16a) shows the relation of wave functions between two neigh-

boring unit cells. The eigenvalue of the matrix in Equation (S16a) is the ratio of wave functions between two neighboring unit cells:

$$\lambda_1 = 1 - \sqrt{2}, \quad \lambda_2 = 1 + \sqrt{2},$$

where $\lambda_2 > 1$ is unphysical for edge states. The eigenvector associated with λ_1 is $(\sqrt{2} + 1, -\sqrt{2})^T$, and combining it with Equations (S16b) and (S16c) we can fix the wave functions within the same unit cell i :

$$\psi_{i,2}^o : \psi_{i,4}^o : \psi_{i,6}^o : \psi_{i,8}^o = (\sqrt{2} + 1) : (-\sqrt{2}) : (\sqrt{2} - 1) : (1 - \sqrt{2}), \quad i \in N_+. \quad (\text{S17})$$

This relation also indicates $\psi_{1,2}^o : \psi_{1,4}^o = x : (-1 - x) = (\sqrt{2} + 1) : (-\sqrt{2})$, which gives

$$x = -\sqrt{2} - 1. \quad (\text{S18})$$

Substituting the value of x into the upper panel of Figure S7D and considering the decay ratio λ_1 , the analytical solution for the edge state can be obtained, as shown in the upper panel of Figure S7B with a normalization of wave function. We can see that the zero-energy edge mode with odd mirror symmetry dominates on the concave region, which explains the distribution of wave function of the HHGY in the upper panel Figure S7A.

In order to obtain the analytical solution of the zero-energy edge mode with even mirror symmetry, we draw the schematic structure for derivation in the lower panel of Figure S7C. Similarly, we only need to consider the wave functions of ten sites in one unit cell due to the mirror symmetry. For the zero energy state with even mirror symmetry, we have

$$\psi_{i,2}^e = \psi_{i,9}^e = 0, \quad i \in N \quad (\text{S19})$$

with the superscript “e” denoting even mirror symmetry and i labeling the unit cell. Starting

with $\psi_{0,1}^e = 1$, the relations of wave functions at the following sites can be derived for the zero-energy mode:

$$\begin{aligned}
(\text{site } 0, 2) \quad \psi_{0,3}^e &= -\psi_{0,1}^e = -1, \\
(\text{site } 0, 3) \quad \psi_{0,4}^e &= -\psi_{0,2}^e = 0, \\
(\text{site } 0, 4) \quad \psi_{0,5}^e &= -\psi_{0,3}^e = 1, \\
(\text{site } 0, 5) \quad \psi_{0,6}^e &= -\psi_{0,4}^e = 0.
\end{aligned} \tag{S20}$$

Similarly, starting with $\psi_{1,1}^e = y$, we have the relations of wave functions at the following sites:

$$\begin{aligned}
(\text{site } 1, 2) \quad \psi_{1,3}^e &= -\psi_{1,1}^e = -y, \\
(\text{site } 0, 6) \quad \psi_{0,7}^e &= -\psi_{0,5}^e - \psi_{1,3}^e = y - 1, \\
(\text{site } 1, 3) \quad \psi_{1,4}^e &= -\psi_{0,6}^e - \psi_{1,2}^e = 0, \\
(\text{site } 0, 7) \quad \psi_{0,8}^e &= -\psi_{0,6}^e = 0, \\
(\text{site } 1, 4) \quad \psi_{1,5}^e &= -\psi_{1,3}^e = y, \\
(\text{site } 0, 8) \quad \psi_{0,9}^e &= -\psi_{0,7}^e - \psi_{1,5}^e = 1 - 2y.
\end{aligned} \tag{S21}$$

Since we already know $\psi_{0,9}^e = 0$, combining it with the last line of Equation (S21) we obtain

$$y = 1/2 \tag{S22}$$

For site 5 in 1st unit cell and site 9 in 0th unit cell, the relations are

$$\begin{aligned}
(\text{site } 1, 5) \quad \psi_{1,6}^e &= -\psi_{0,8}^e - \psi_{1,4}^e = 0, \\
(\text{site } 0, 9) \quad \psi_{0,10}^e &= -\psi_{0,8}^e - \psi_{2,2}^e = 0.
\end{aligned} \tag{S23}$$

Finally, setting $\psi_{2,1}^e = z$, we have the relations of wave functions at the following sites:

$$\begin{aligned}
(\text{site } 2, 2) \quad \psi_{2,3}^e &= -\psi_{0,9}^e - \psi_{2,1}^e = -z, \\
(\text{site } 1, 6) \quad \psi_{1,7}^e &= -\psi_{1,5}^e - \psi_{2,3}^e = z - y, \\
(\text{site } 2, 3) \quad \psi_{2,4}^e &= -\psi_{1,6}^e - \psi_{2,2}^e = 0, \\
(\text{site } 1, 7) \quad \psi_{1,8}^e &= -\psi_{1,6}^e = 0, \\
(\text{site } 2, 4) \quad \psi_{2,5}^e &= -\psi_{2,3}^e = z, \\
(\text{site } 1, 8) \quad \psi_{1,9}^e &= -\psi_{1,7}^e - \psi_{2,5}^e = y - 2z.
\end{aligned} \tag{S24}$$

Combining the known $\psi_{1,9}^e = 0$ and the last line of Equation (S24), we obtain

$$z = y/2 = 1/4. \tag{S25}$$

From Equations (S21), (S22), (S24) and (S25) we can find the decay ratio of wave functions between two neighboring unit cells are $z/y = 1/2$. With all the parameters obtained above, the analytical solution for the zero-energy mode with even mirror symmetry can be derived, as shown in the lower panel of Figure S7B, where a normalization of wave function is considered. The zero-energy edge state with even mirror symmetry dominates on the outmost carbon chain of the edge, which explains the distribution of wave function in the lower panel of Figure S7A.

References

- (S1) Kresse, G.; Furthmüller, J. Efficient Iterative Schemes for Ab Initio Total-Energy Calculations Using a Plane-Wave Basis Set. *Phys. Rev. B* **1996**, *54*, 11169–11186.
- (S2) Kresse, G.; Joubert, D. From Ultrasoft Pseudopotentials to the Projector Augmented-Wave Method. *Phys. Rev. B* **1999**, *59*, 1758–1775.

- (S3) Perdew, J. P.; Burke, K.; Ernzerhof, M. Generalized Gradient Approximation Made Simple. *Phys. Rev. Lett.* **1996**, *77*, 3865–3868.
- (S4) Wang, V.; Xu, N.; Liu, J.-C.; Tang, G.; Geng, W.-T. VASPKIT: A User-Friendly Interface Facilitating High-Throughput Computing and Analysis Using VASP Code. *Computer Physics Communications* **2021**, *267*, 108033.
- (S5) Liu, X.; Cho, S. M.; Lin, S.; Chen, Z.; Choi, W.; Kim, Y.-M.; Yun, E.; Baek, E. H.; Ryu, D. H.; Lee, H. Constructing Two-Dimensional Holey Graphyne with Unusual Annulative π -Extension. *Matter* **2022**, *5*, 2306–2318.
- (S6) Pizzi, G. et al. Wannier90 as a Community Code: New Features and Applications. *J. Phys. Condens. Matter* **2020**, *32*, 165902.
- (S7) Yu, R.; Qi, X. L.; Bernevig, A.; Fang, Z.; Dai, X. Equivalent Expression of Z_2 Topological Invariant for Band Insulators Using the Non-Abelian Berry Connection. *Phys. Rev. B* **2011**, *84*, 75119.
- (S8) Weng, H.; Yu, R.; Hu, X.; Dai, X.; Fang, Z. Quantum Anomalous Hall Effect and Related Topological Electronic States. *Adv. Phys.* **2015**, *64*, 227–282.
- (S9) Cano, J.; Bradlyn, B.; Wang, Z.; Elcoro, L.; Vergniory, M. G.; Felser, C.; Aroyo, M. I.; Bernevig, B. A. Topology of Disconnected Elementary Band Representations. *Phys. Rev. Lett.* **2018**, *120*, 266401.
- (S10) Po, H. C.; Watanabe, H.; Vishwanath, A. Fragile Topology and Wannier Obstructions. *Phys. Rev. Lett.* **2018**, *121*, 126402.
- (S11) Wu, L.-H.; Hu, X. Scheme for Achieving a Topological Photonic Crystal by Using Dielectric Material. *Phys. Rev. Lett.* **2015**, *114*, 223901.
- (S12) Kariyado, T.; Jiang, Y.-C.; Yang, H.; Hu, X. Counterpropagating Topological Interface

States in Graphene Patchwork Structures with Regular Arrays of Nanoholes. *Phys. Rev. B* **2018**, *98*, 195416.

(S13) Kariyado, T.; Hu, X. Topological States Characterized by Mirror Winding Numbers in Graphene with Bond Modulation. *Sci. Rep.* **2017**, *7*, 16515.

(S14) Bernevig, B. A.; Hughes, T. L.; Zhang, S.-C. Quantum Spin Hall Effect and Topological Phase Transition in HgTe Quantum Wells. *Science* **2006**, *314*, 1757–1761.